Batteries

Activating Inert Metallic Compounds for High-Rate Lithium–Sulfur Batteries Through In Situ Etching of Extrinsic Metal

Meng Zhao+, Hong-Jie Peng+, Ze-Wen Zhang, Bo-Quan Li, Xiao Chen, Jin Xie, Xiang Chen, Jun-Yu Wei, Qiang Zhang, and Jia-Qi Huang*

Abstract: Surface reactions constitute the foundation of various energy conversion/storage technologies, such as the lithium–sulfur (Li-S) batteries. To expedite surface reactions for high-rate battery applications demands in-depth understanding of reaction kinetics and rational catalyst design. Now an in situ extrinsic-metal etching strategy is used to activate an inert monometal nitride of hexagonal Ni_3N through iron-incorporated cubic Ni_3FeN. In situ etched Ni_3FeN regulates polysulfide-involving surface reactions at high rates. Electron microscopy was used to unveil the mechanism of in situ catalyst transformation. The Li-S batteries modified with Ni_3FeN exhibited superb rate capability, remarkable cycling stability at a high sulfur loading of $4.8\ mg\,cm^{-2}$, and lean-electrolyte operability. This work opens up the exploration of multimetallic alloys and compounds as kinetic regulators for high-rate Li-S batteries and also elucidates catalytic surface reactions and the role of defect chemistry.

Surface and interfacial reactions play an essential role in defining various energy-transforming processes, such as solar fuel production and electrochemical energy storage.[1] Today's growing demand for intermittent and discrete energy storage drives the exploration of emerging battery chemistries, such as lithium–sulfur (Li-S) and lithium–air batteries, which often rely on reversible surface electrochemical reactions to afford a high energy density.[2] Expediting these reactions enables the devices with favorable rate performance but often requires reaction mechanism with intrinsically fast kinetics. If the surface reaction mechanism can be in-depth excavated, energy chemistries and related technologies will be advanced expectedly.

As a promising substituent to lithium-ion batteries, Li-S batteries afford an attractive specific energy of 2600 Wh kg^{-1} in theory.[3,4] Among various strategies, introducing electrocatalytically active components to the sulfur cathode is recently regarded as an efficient and effective way to accelerate the surface reaction kinetics.[5–8] Rapid surface reactions simultaneously contribute to improving sulfur utilization and mitigating the shuttle effect of soluble polysulfide intermediates, which is often considered as the major origin of capacity fading.[9,10] However, the actual active phases of currently developed electrocatalysis in working conditions have hardly been vigorously validated. Owing to the lack of rational understanding, it is usually by the Edisonian approach to explore new electrocatalysts, rendering the exploration time-consuming and non-precise.[11]

Modern surface science indicates that the catalytic activity often originates from the surface or subsurface defects and vacancies of a solid catalyst.[8,12] Such a general understanding enlightens us to investigate the role of vacancy in electrocatalysis for Li-S batteries and extract core design principles of catalyst design. Thereafter, to explore novel catalysts for polysulfide redox reaction, to enlarge their groups, and to optimize their properties can be realized through composition, phase, and site engineering based on above rationales.

Herein, we demonstrate that the introduction of an extrinsic metal to a monometallic compound, similar to the alloying strategy for metal catalyst design,[13] activates the originally inert phase for kinetic propelling of polysulfide-involving surface reactions at a high rate. Hexagonal nickel nitride (Ni_3N), selected as a proof-of-concept pre-catalyst, was found poorly active for polysulfide mediating, which was transformed into highly active cubic nickel–iron nitride (Ni_3FeN) phase after the incorporation of iron. Both compounds are conductive,[14,15] but the more electropositive iron (compared to nickel) at the corner sites, inclines to be leached out through polysulfide etching, leaving abundant vacant defects around the nickel site to activate it.

Ni_3N and Ni_3FeN nanoparticles were synthesized by ammonolysis (Supporting Information, Figure S1a,b). Both Ni_3N and Ni_3FeN are found as nanoparticles of 10–30 nm in size, supported on wrinkled graphene sheets (denoted as Ni_3N/G and Ni_3FeN/G, respectively). The X-ray diffraction patterns of Ni_3N and Ni_3FeN samples indicate their distinct crystal structures: a hexagonal phase for Ni_3N (JCPDS No. 10-0280, $a = b = 4.621$ Å; $c = 4.304$ Å),[16] and a cubic phase for Ni_3FeN (JCPDS No. 50-1434, $a = b = c = 3.760$ Å; Supporting Information, Figure S1c).[15] The incorporation of iron induces the hexagonal-to-cubic phase transformation. Transmission electron microscopy (TEM) images further indicate

[*] M. Zhao,[+] J.-Y. Wei, Prof. J.-Q. Huang
School of Materials Science and Engineering
Beijing Institute of Technology
Beijing 100081 (P. R. China)
E-mail: jqhuang@bit.edu.cn

M. Zhao,[+] J.-Y. Wei, Prof. J.-Q. Huang
Advanced Research Institute of Multidisciplinary Science
Beijing Institute of Technology
Beijing 100081 (P. R. China)

Dr. H.-J. Peng,[+] Z.-W. Zhang, B.-Q. Li, X. Chen, J. Xie, X. Chen,
Prof. Q. Zhang
Department of Chemical Engineering, Tsinghua University
Beijing 100084 (P. R. China)

[+] These authors contributed equally to this work.

Supporting information and the ORCID identification number(s) for the author(s) of this article can be found under:
https://doi.org/10.1002/anie.201812062.

well-indexed lattice fringes with a *d*-spacing of 0.292 nm for the (101) plane of Ni_3N and 0.217 nm for the (111) plane of Ni_3FeN, respectively (Supporting Information, Figure S1d,e).

X-ray photoelectron spectroscopy (XPS) was carried out on Ni_3FeN and Ni_3N before and after reacting with polysulfides to probe their interaction with polysulfides. The incorporation of iron increases the electron density around nickel and nitrogen, inducing obvious red-shifts of Ni^0 $2p_{3/2}$ peaks (from 852.7 eV to 852.0 eV) and N 1s peaks (from 397.8 eV to 396.9 eV) (Figure 1 a and b).[17] The presence of Ni^{2+} can be ascribed to the inevitable oxidation of surface layer (Figure 1a).[15]
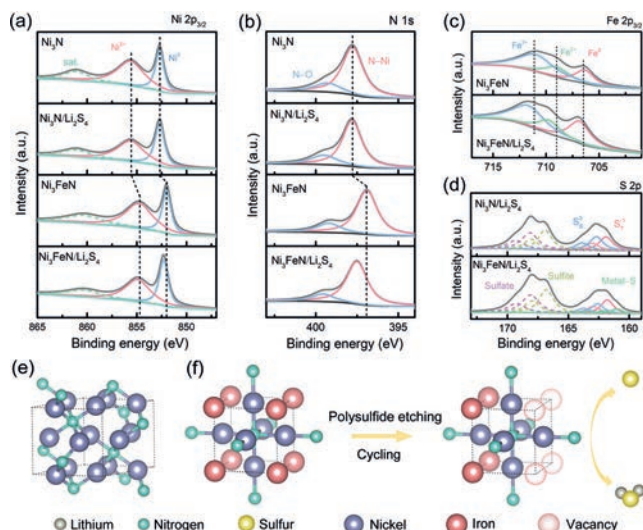
Figure 1. Illustration of the polysulfide-etching-induced activation mechanism. Refined a) Ni 2p, b) N 1s, c) Fe 2p, and d) S 2p XPS spectra of different samples with or without Li_2S_4 addition. e) Atomic structure model of hexagonal Ni_3N. f) Atomic structure model of cubic Ni_3FeN and illustration of the polysulfide etching process toward an active $Ni_3Fe_{1−δ}N$ phase.

Static adsorption of Li_2S_4 by Ni_3FeN/G and Ni_3N/G aims to simulate the working environment in batteries. A nearly colorless solution after 3.0 h adsorption with Ni_3FeN/G, and a pale yellow solution with Ni_3N/G, imply stronger interaction between polysulfides and Ni_3FeN than Ni_3N (Supporting Information, Figure S2). It can be easily deduced that the more electropositive iron strengthens the adsorption to negatively charged terminal sulfur (S_T) in polysulfides, which is confirmed by the blue-shifts of 0.5 eV for all peaks in the Fe $2p_{3/2}$ spectrum of Ni_3FeN after polysulfide adsorption (denoted as Ni_3FeN/Li_2S_4 and the same for Ni_3N/Li_2S_4), indicating the electron transfer from Fe to S_T (Figure 1 c).

Nevertheless, the effects of extrinsic iron are more than electropositivity. Neither the Ni $2p_{3/2}$ nor N 1s spectrum of Ni_3N/Li_2S_4 exhibits any change compared to that of pristine Ni_3N, indicating no spectroscopically validated chemisorption (Figure 1a,b). The Ni−N plane of Ni_3N is inert toward polysulfides because of the full coordination of Ni−N in the bulk hexagonal phase, rendering binding sites only available on the surface (Figure 1e). With iron incorporation, the originally inert Ni−N plane turns into strongly binding toward

polysulfides, as indicated by the significant blue-shifts in Ni $2p_{3/2}$ (0.3 eV) and N 1s (0.6 eV) spectra of Ni_3FeN/Li_2S_4 compared to Ni_3FeN (Figure 1 a,b). These blue-shifts suggest the electron transfer from Ni-N to the S_T plane.

The aforementioned difference in interaction paradigm is also validated by the S 2p spectra. Pristine Li_2S_4 exhibited typical $2p_{3/2}/2p_{1/2}$ doublets in the S 2p spectrum at 162.3 and 163.2 eV (referring to $2p_{3/2}$ peaks), attributing to S_T and bridging sulfur (S_B), respectively (Supporting Information, Figure S4).[18] Extra peaks (166.8–169.3 eV) result from oxidation during sample preparation.[19] Ni_3N/Li_2S_4 hardly exhibits a change in the S 2p spectrum (Figure 1 d). In contrast, a new peak at 161.0 eV emerges in the S 2p spectrum of Ni_3FeN/Li_2S_4 and is attributed to the formation of a sulfur–metal (that is, iron and nickel) bond.

Based on above observation, it is speculated that extrinsic iron activates the inert Ni−N plane through a polysulfide-etching-induced vacancy-formation mechanism (Figure 1 f). Iron atoms at the corner sites of cubic structure are leached out via polysulfide etching, as iron is more electropositive than nickel to react with S_T. The removal of iron results in a metastable cubic $Ni_3Fe_{1−δ}N$ phase ($δ$ refers to the stoichiometric number of vacancies left by iron), which is further stabilized through trapping polysulfides within the vacant defects of $Ni_3Fe_{1−δ}N$.

Subsequent post-mortem analysis provides further evidence for the above mechanism. As shown in the high-angle annular dark-field scanning transmission electron microscopy (HAADF-STEM) image and corresponding elemental mappings, pristine Ni_3FeN particles exhibit uniform distribution of nickel and iron (Figure 2 a). The linear scan further indicates the overlap of two elements with a small deviation in spatial distribution (Figure 2 b). However, the cycled Ni_3FeN particles are shown with abnormally surface-enriched iron element, implying the phase migration after polysulfide etching (Figure 2 c,d). The migrated species is further identified as a new phase of ferrous sulfide (FeS; Supporting Information, Figure S5), while the cycled Ni_3N sample remains its original phase (Supporting Information, Figure S6). The phase migration is ascribed to the Kirkendall effect and indicates the reaction between polysulfides and Ni_3FeN.
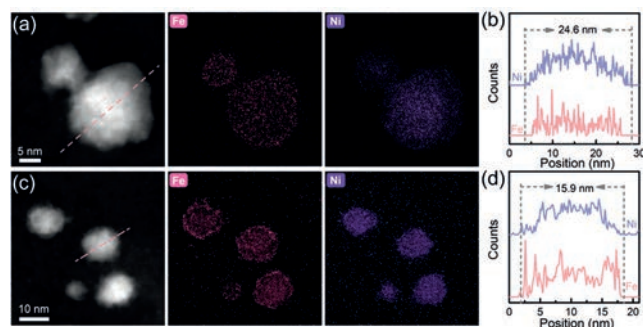
Figure 2. a) HAADF-STEM image of Ni_3FeN-G and the corresponding EDS element distribution. b) Linear elemental distribution of the particle marked in (a). c) HAADF-STEM images of Ni_3FeN-G and the corresponding EDS element distribution after 5 cycles at 0.5 C. d) Linear elemental distribution of the particle marked in (c).

Kinetics of liquid–solid and liquid–liquid reactions were probed to elucidate the effect of extrinsic metal incorporation/removal. Following previous reports,[20] chronoamperometry was employed to probe the liquid–solid nucleation behaviors of lithium sulfide (Li_2S) on various hosts, that is, G, Ni_3N/G, and Ni_3FeN/G (Figure 3a). All three cells reached the highest potentiostatic current after approximately 3500 s, but the integral areas of current peaks varied significantly,
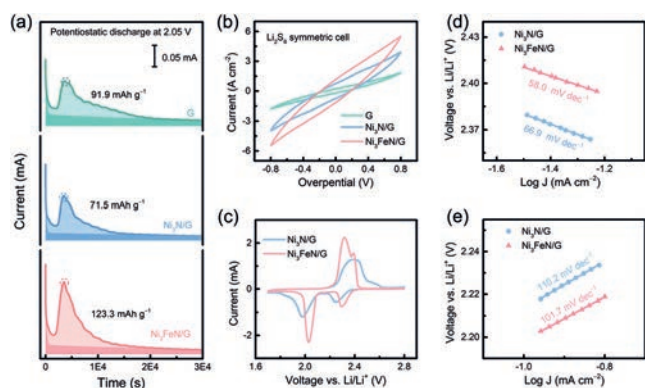
Figure 3. Electrochemical kinetics. a) Chronoamperometry curves of Li_2S_8/tetraglyme solution discharged at 2.05 V on different surfaces. The lighter and darker colored regions indicate the precipitation of Li_2S and the reduction of Li_2S_8/Li_2S_6, respectively. b) CV curves of Li_2S_6 symmetric cells employing different scaffolds as current collectors. c) CV curves of Li-S cells applying a Ni_3N/G- and Ni_3FeN/G-modified separator, respectively. Corresponding Tafel plots for d) the first reduction peak and e) the oxidation peak.

resulting in Li_2S nucleation capacities of 92, 72, and 123 mAh g^{-1} on G, Ni_3N/G, and Ni_3FeN/G, respectively. As the electrode is of equal mass, the sacrifice in surface area for solid precipitation led to small capacity for Ni_3N/G. However, because of the modulation of iron, Ni_3FeN-derived $Ni_3Fe_{1-\delta}N$/G enabled substantially more electrodeposition despite the smaller surface area than G. The morphology characterization of electrodes also reveals that unlike on G and Ni_3N/G, deposited Li_2S layer on Ni_3FeN/G is much thicker, featuring a three-dimensional growth characteristic (Supporting Information, Figure S8).

The liquid–liquid reactions were probed using symmetric cells with a Li_2S_6 electrolyte for cyclic voltammetry (CV) and electrochemical impedance measurements.[21] The redox current responses at a voltage bias of 0.8 V increase in the order of $G < Ni_3N/G < Ni_3FeN/G$ (Figure 3b), while trends in electrochemical impedance has a reverse sequence (Supporting Information, Figure S7). Furthermore, the redox current of FeS/G is comparable to G, further indicating that the active center in Ni_3FeN is mainly the vacancy rather than the iron site on FeS (Supporting Information, Figure S10). These results indicate that the highest charge-transfer rate is between polysulfides and Ni_3FeN/G, which is attributed to stronger ability of vacancies in etched $Ni_3Fe_{1-\delta}N$ to adsorb polysulfides than fully coordinated compounds.

The kinetic-regulating role of $Ni_3Fe_{1-\delta}N$ after iron removal was further demonstrated in actual Li-S batteries.

Owing to previous success of modified separators in enhancing Li-S batteries,[18,22] Ni_3FeN/G and Ni_3N/G were filtrated on separators as a catalytic membrane (Supporting Information, Figure S11). The areal sulfur loading is 1.2 mg cm^{-2}, while the loading of Ni_3FeN/G or Ni_3N/G is 0.3 mg cm^{-2}. The CV curves of as-assembled Li-S cells exhibit typical redox peaks: the two cathodic peaks at 2.2–2.3 and 1.9–2.1 V, corresponding to the formation of soluble polysulfides and solid Li_2S, respectively, and two anodic peaks that are partially overlapped, indicating the sequential oxidation of Li_2S and polysulfides (Figure 3c). Compared to non-activated Ni_3N/G, the cell with Ni_3FeN/G possessed less severe polarization for all redox peaks, suggesting better kinetics. Along with the smaller impedance (Supporting Information, Figure S12), the kinetics enhancement is ascribed to the rapid charge transfer between the $Ni_3Fe_{1-\delta}N$ mediator and adsorbed polysulfides.

For quantitative analysis, Tafel plots of the first reduction and oxidation processes are obtained, respectively (Figure 3d,e).[5] The second reduction process was not considered owing to the continuous background current induced by polysulfide interconversion until the onset potential of Li_2S nucleation. For the first reduction, the fitted Tafel slopes of Ni_3FeN/G and Ni_3N/G cells are 58.0 and 66.9 mV dec^{-1}, respectively (Figure 3d); while for the first oxidation, they are 102 and 110 mV dec^{-1}, respectively (Figure 3e). The smaller Tafel slopes for Ni_3FeN/G cell indicate more facile reactions between liquid polysulfides and solid sulfur/Li_2S under the regulation of $Ni_3Fe_{1-\delta}N$ than Ni_3N. Besides, corresponding onset potentials for $Ni_3Fe_{1-\delta}N$-mediated polysulfide redox are about 37 mV positive for sulfur reduction and about 16 mV negative for Li_2S oxidation, also demonstrating the high catalytic activity of $Ni_3Fe_{1-\delta}N$ after iron incorporation/removal.

The rapid polysulfide redox reactions mediated by in situ etched Ni_3FeN provide the Li-S batteries with a superb rate performance (Figure 4a). The cell with a Ni_3FeN/G-modified separator delivered high average capacities of 1309, 1144, 1047, 974, and 905 mAh g^{-1} at 0.1, 0.2, 0.5, 1, and 2 C (1 C = 1672 mAh g^{-1}), which are 9–14% and 11–31% higher than those of Ni_3N/G and FeS/G (Supporting Information, Figure S13). At a high rate of 3 C (6.0 mA cm^{-2}), the Ni_3FeN cell still maintained a high capacity of 822 mAh g^{-1}, while the Ni_3N and FeS cell lost its low discharge plateau. Such a phenomenon is in accordance with the liquid–solid kinetic study, where the Ni_3FeN is shown to improve the Li_2S nucleation rate significantly through strong-binding vacancy sites but the nucleation overpotential on inert Ni_3N at such a high rate is too large to be met by cutoff voltage, leading to early termination of discharge.

The above argument is further validated by galvanostatic discharge–charge profiles (Figure 4b). At a low current density of 0.1 C, the discharge voltages of both cells are comparable despite the higher capacity of the Ni_3FeN cell. However, unlike the smooth transition for the Ni_3FeN cell, the discharge profile of Ni_3N cell exhibits a huge and trailing voltage "dip" at a high rate of 2 C, indicating the sluggish kinetics of Li_2S nucleation/growth on inert Ni_3N and graphene surfaces. Therefore, the sudden capacity decrease for the Ni_3N
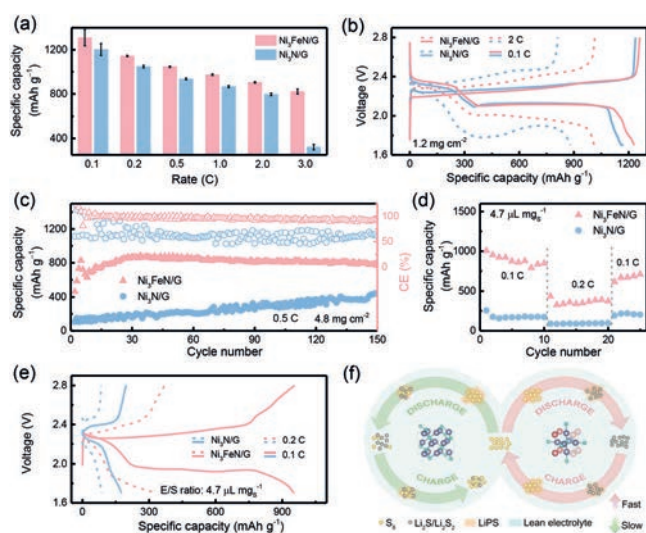
Figure 4. Li-S battery performances. a) Rate performance and b) galvanostatic discharge–charge profiles at different current densities. c) Cycling performance of high-sulfur-loading batteries at 0.5 C. d) Rate performance and e) galvanostatic discharge–charge profiles of lean-electrolyte batteries. Sulfur loading ($mg_{(sulfur)} cm^{-2}$): a),b) 1.2; c)–e) 4.8. E/S ratio ($\mu L_{(electrolyte)} mg_{(sulfur)}^{-1}$): a),b) 16; c) 14; d),e) 4.7. f) Illustration of Li-S reaction scenarios with different catalysts under lean-electrolyte conditions.

cell at 3 C is expected. Further to Li_2S formation, the incorporation/removal of iron in Ni_3FeN also has a profound influence on Li_2S oxidation. The Ni_3FeN cell generally possessed a barrierless feature at the beginning of charge at both 0.1 and 2 C; while the Ni_3N cell still suffered from an initial charge barrier. Similar to discharge, such a difference is in agreement with Tafel slopes (Figure 3e).

Kinetic regulation enabled by an electrolyte has previously been shown to improve cycling stability of Li-S batteries.[6,10] In this sense, the Ni_3FeN/G cell preserved its 78% of initial capacity after 180 cycles at 1 C, higher than 69% and 54% for the Ni_3N/G cell and the G cell, respectively (Supporting Information, Figures S14 and S15a). Ni_3FeN/G also enabled the cell to be cycled at a 3 C for more than 150 cycles while G and Ni_3N/G could not (Supporting Information, Figure S16a). This can be attributed to the shuttle mitigation by a Ni_3FeN/G separator as the lithium anode with Ni_3FeN/G preserved its morphological compactness mostly when compared to those with G and Ni_3N/G (Supporting Information, Figure S17). Considering the very low mass ratio of Ni_3FeN to sulfur (approximately 1:100 based on thermogravimetric analysis), it is kinetically regulated shuttle "bypassing" rather than chemisorption that accounts for enhanced battery stability.[9]

To further demonstrate the high activity of Ni_3FeN for polysulfide catalysis with an extremely low mass ratio of Ni_3FeN to sulfur (1:400), high-loading cathodes (sulfur loading: 4.8 $mg cm^{-2}$) were tested. After an activation process induced by sulfur redistribution,[23] Ni_3FeN/G enabled the sulfur cathode to achieve maximum capacities of 1103 and 900 $mAh g^{-1}$ at 0.2 and 0.5 C, along with capacity retention of 75% and 89% after 150 cycles, respectively (Supporting

Information, Figure S16b; Figure 4c). In contrast, the control G and Ni_3N/G cells delivered much lower capacities with strong fluctuation of Coulombic efficiencies, suffering from low sulfur utilization and severe shuttle effect at high current densities (Figure 4c; Supporting Information, Figure S15b). Ni_3FeN/G catalyzed Li-S battery has higher rate performance and area capacity, even compared to the recently reported high-sulfur-loading performance (Supporting Information, Table S1).

All of the above electrochemical tests were carried out with substantial excess of electrolyte (electrolyte/sulfur (E/S) ratios of 14–16 $\mu L_{(electrolyte)} mg_{(sulfur)}^{-1}$), which is detrimental to the device energy density.[4] Therefore, it is necessary to evaluate the electrocatalyst at a lean-electrolyte condition.[24] At a low E/S ratio of 4.7 $\mu L_{(electrolyte)} mg_{(sulfur)}^{-1}$, the Ni_3FeN/G cell delivered high capacities of 1007 and 438 $mAh g^{-1}$ at 0.1 and 0.2 C, 3.9 (4.6) and 4.8 (6.2) times than those of Ni_3N/G (FeS/G) (Figure 4d; Supporting Information, Figure S18a). Similar to that at high rates (> 2 C), lean-electrolyte cells exhibit typical charge–discharge curves with Ni_3FeN/G but lose the low discharge plateau with Ni_3N/G and FeS/G (Figure 4e; Supporting Information, Figure S18b). The lean-electrolyte cell evaluation again illustrates the pivotal role of iron incorporation/removal in regulating reactions at harsh working conditions as the vacancy-rich $Ni_3Fe_{1-\delta}N$ phase strengthens the intermediate binding, lowers the reaction barriers, and thus drives more complete sulfur/polysulfide/Li_2S conversion than Ni_3N (Figure 4f).

In summary, we have demonstrated a strategy to activate inert Ni_3N for polysulfide catalysis in Li-S batteries. With the assist from advanced characterization tools such as HAADF-STEM, it was validated that introducing an extrinsic metal (that is, iron) in the Ni_3N triggered the hexagonal-to-cubic phase transformation and this metal can be leached out in situ via polysulfide etching, rendering a highly active vacancy-rich phase to promote the kinetics of polysulfide-involving surface reactions. The Li-S batteries catalyzed by Ni_3FeN exhibited superb rate performance, with a capacity of 822 $mAh g^{-1}$ at 3 C, remarkable cycling stability at a high sulfur loading of 4.8 $mg cm^{-2}$ (89% capacity retention after 150 cycles), and lean-electrolyte operability. This work not only describes an extrinsic-metal activation mechanism for non-active monometal compounds but also elucidates the important role of in situ phase evolution and vacancy formation in regulating catalytic reactions. Therefore, this work opens up the exploration of multimetallic alloys and compounds for Li-S battery kinetics regulation and also enlighten understanding of surface reactions and catalyst design.

Acknowledgements

Conflict of interest

The authors declare no conflict of interest.

[1] J. H. Montoya, L. C. Seitz, P. Chakthranont, A. Vojvodic, T. F. Jaramillo, J. K. Norskov, *Nat. Mater.* **2017**, *16*, 70–81; N. S. Choi, Z. H. Chen, S. A. Freunberger, X. L. Ji, Y. K. Sun, K. Amine, G. Yushin, L. F. Nazar, J. Cho, P. G. Bruce, *Angew. Chem. Int. Ed.* **2012**, *51*, 9994–10024; *Angew. Chem.* **2012**, *124*, 10134–10166.

[2] P. G. Bruce, S. A. Freunberger, L. J. Hardwick, J. M. Tarascon, *Nat. Mater.* **2012**, *11*, 19–29.

[3] Y. X. Yin, S. Xin, Y. G. Guo, L. J. Wan, *Angew. Chem. Int. Ed.* **2013**, *52*, 13186–13200; *Angew. Chem.* **2013**, *125*, 13426–13441; Q. Pang, X. Liang, C. Y. Kwok, L. F. Nazar, *Nat. Energy* **2016**, *1*, 16132; H. J. Peng, J. Q. Huang, X. B. Cheng, Q. Zhang, *Adv. Energy Mater.* **2017**, *7*, 1700260; S. M. Xu, D. W. McOwen, L. Zhang, G. T. Hitz, C. W. Wang, Z. H. Ma, C. J. Chen, W. Luo, J. Q. Dai, Y. D. Kuang, E. M. Hitz, K. Fu, Y. H. Gong, E. D. Wachsman, L. B. Hu, *Energy Storage Mater.* **2018**, https://doi.org/10.1016/j.ensm.2018.1008.1009.

[4] R. P. Fang, S. Y. Zhao, Z. H. Sun, W. Wang, H. M. Cheng, F. Li, *Adv. Mater.* **2017**, *29*, 1606823; S. H. Chung, C. H. Chang, A. Manthiram, *Adv. Funct. Mater.* **2018**, *28*, 1801188.

[5] H. Al Salem, G. Babu, C. V. Rao, L. M. R. Arava, *J. Am. Chem. Soc.* **2015**, *137*, 11542–11545.

[6] Z. Yuan, H. J. Peng, T. Z. Hou, J. Q. Huang, C. M. Chen, D. W. Wang, X. B. Cheng, F. Wei, Q. Zhang, *Nano Lett.* **2016**, *16*, 519–527.

[7] Z. H. Sun, J. Q. Zhang, L. C. Yin, G. J. Hu, R. P. Fang, H. M. Cheng, F. Li, *Nat. Commun.* **2017**, *8*, 14627; G. M. Zhou, H. Z. Tian, Y. Jin, X. Y. Tao, B. F. Liu, R. F. Zhang, Z. W. Seh, D. Zhuo, Y. Y. Liu, J. Sun, J. Zhao, C. X. Zu, D. S. Wu, Q. F. Zhang, Y. Cui, *Proc. Natl. Acad. Sci. USA* **2017**, *114*, 840–845; T. G. Jeong, D. S. Choi, H. Song, J. Choi, S. A. Park, S. H. Oh, H. Kim, Y. Jung, Y. T. Kim, *ACS Energy Lett.* **2017**, *2*, 327–333; H. D. Yuan, X. L. Chen, G. M. Zhou, W. K. Zhang, J. M. Luo, H. Huang, Y. P. Gan, C. Liang, Y. Xia, J. Zhang, J. G. Wang, X. Y. Tao, *ACS Energy Lett.* **2017**, *2*, 1711–1719; Y. R. Zhong, L. C. Yin, P. He, W. Liu, Z. S. Wu, H. L. Wang, *J. Am. Chem. Soc.* **2018**, *140*, 1455–1459; J. C. Ye, J. J. Chen, R. M. Yuan, D. R. Deng, M. S. Zheng, L. Cronin, Q. F. Dong, *J. Am. Chem. Soc.* **2018**, *140*, 3134–3138; J. T. Zhang, Z. Li, Y. Chen, S. Y. Gao, X. W. Lou, *Angew. Chem. Int. Ed.* **2018**, *57*, 10944–10948; *Angew. Chem.* **2018**, *130*, 11110–11114; L. Luo, S. H. Chung, H. Y. Asl, A. Manthiram, *Adv. Mater.* **2018**, *30*, 1804149; C. Luo, H. L. Zhu, W. Luo, F. Shen, X. L. Fan, J. Q. Dai, Y. J. Liang, C. S. Wang, L. B. Hu, *ACS Appl. Mater. Interfaces* **2017**, *9*, 14801–14807; D. R. Deng, F. Xue, Y. J. Jia, J. C. Ye, C. D. Bai, M. S. Zheng, Q. F. Dong, *ACS Nano* **2017**, *11*, 6031–6039; Y. Zhong, D. L. Chao, S. J. Deng, J. Y. Zhan, R. Y. Fang, Y. Xia, Y. D. Wang, X. L. Wang, X. H. Xia, J. P. Tu, *Adv. Funct. Mater.* **2018**, *28*, 1706391; L. L. Zhang, X. Chen, F. Wan, Z. Q. Niu, Y. J. Wang, Q. Zhang, J. Chen, *ACS Nano* **2018**, *12*, 9578–9586; T. H. Zhou, W. Lv, J. Li,

[8] H. B. Lin, L. Q. Yang, X. Jiang, G. C. Li, T. R. Zhang, Q. F. Yao, G. W. Zheng, J. Y. Lee, *Energy Environ. Sci.* **2017**, *10*, 1476–1486.

[9] H. J. Peng, Q. Zhang, *Angew. Chem. Int. Ed.* **2015**, *54*, 11018–11020; *Angew. Chem.* **2015**, *127*, 11170–11172.

[10] Z. W. Zhang, H. J. Peng, M. Zhao, J. Q. Huang, *Adv. Funct. Mater.* **2018**, *28*, 1707536.

[11] Z. W. Seh, J. Kibsgaard, C. F. Dickens, I. B. Chorkendorff, J. K. Norskov, T. F. Jaramillo, *Science* **2017**, *355*, eaad4998.

[12] D. F. Yan, Y. X. Li, J. Huo, R. Chen, L. M. Dai, S. Y. Wang, *Adv. Mater.* **2017**, *29*, 1606459; H. Li, C. Tsai, A. L. Koh, L. L. Cai, A. W. Contryman, A. H. Fragapane, J. H. Zhao, H. S. Han, H. C. Manoharan, F. Abild-Pedersen, J. K. Norskov, X. L. Zheng, *Nat. Mater.* **2016**, *15*, 48–54.

[13] J. Greeley, T. F. Jaramillo, J. Bonde, I. B. Chorkendorff, J. K. Norskov, *Nat. Mater.* **2006**, *5*, 909–913.

[14] K. Xu, P. Z. Chen, X. L. Li, Y. Tong, H. Ding, X. J. Wu, W. S. Chu, Z. M. Peng, C. Z. Wu, Y. Xie, *J. Am. Chem. Soc.* **2015**, *137*, 4119–4125.

[15] X. D. Jia, Y. F. Zhao, G. B. Chen, L. Shang, R. Shi, X. F. Kang, G. I. N. Waterhouse, L. Z. Wu, C. H. Tung, T. R. Zhang, *Adv. Energy Mater.* **2016**, *6*, 1502585.

[16] D. Q. Gao, J. Y. Zhang, T. T. Wang, W. Xiao, K. Tao, D. S. Xue, J. Ding, *J. Mater. Chem. A* **2016**, *4*, 17363–17369.

[17] B. R. Xia, T. T. Wang, X. Chi, X. J. Yu, P. T. Liu, J. Y. Zhang, S. B. Xi, Y. H. Du, D. Q. Gao, *Appl. Phys. Lett.* **2017**, *111*, 232402.

[18] H. J. Peng, Z. W. Zhang, J. Q. Huang, G. Zhang, J. Xie, W. T. Xu, J. L. Shi, X. Chen, X. B. Cheng, Q. Zhang, *Adv. Mater.* **2016**, *28*, 9551–9558.

[19] X. Liang, C. Y. Kwok, F. Lodi-Marzano, Q. Pang, M. Cuisinier, H. Huang, C. J. Hart, D. Houtarde, K. Kaup, H. Sommer, T. Brezesinski, J. Janek, L. F. Nazar, *Adv. Energy Mater.* **2016**, *6*, 1501636.

[20] F. Y. Fan, W. C. Carter, Y. M. Chiang, *Adv. Mater.* **2015**, *27*, 5203–5209.

[21] H. J. Peng, G. Zhang, X. Chen, Z. W. Zhang, W. T. Xu, J. Q. Huang, Q. Zhang, *Angew. Chem. Int. Ed.* **2016**, *55*, 12990–12995; *Angew. Chem.* **2016**, *128*, 13184–13189.

[22] S. H. Chung, A. Manthiram, *Adv. Funct. Mater.* **2014**, *24*, 5299–5306; H. J. Peng, D. W. Wang, J. Q. Huang, X. B. Cheng, Z. Yuan, F. Wei, Q. Zhang, *Adv. Sci.* **2016**, *3*, 1500268.

[23] X. Q. Yu, H. L. Pan, Y. N. Zhou, P. Northrup, J. Xiao, S. M. Bak, M. Z. Liu, K. W. Nam, D. Y. Qu, J. Liu, T. P. Wu, X. Q. Yang, *Adv. Energy Mater.* **2015**, *5*, 1500072; H. J. Peng, J. Q. Huang, X. Y. Liu, X. B. Cheng, W. T. Xu, C. Z. Zhao, F. Wei, Q. Zhang, *J. Am. Chem. Soc.* **2017**, *139*, 8458–8466.

[24] Y. X. Yang, Y. R. Zhong, Q. W. Shi, Z. H. Wang, K. N. Sun, H. L. Wang, *Angew. Chem. Int. Ed.* **2018**, *57*, 15549–15552; *Angew. Chem.* **2018**, *130*, 15775–15778.